Experimental and kinetic modeling study of PAH formation in methane coflow diffusion flames doped with *n*-butanol

Hanfeng Jin [a,b], Alberto Cuoci [a], Alessio Frassoldati [a], Tiziano Faravelli [a,*], Yizun Wang [b], Yuyang Li [b], Fei Qi [b,c,*]

[a] Department of Chemistry, Materials, and Chemical Engineering, Politecnico di Milano, P.zza Leonardo da Vinci 32, 20133 Milano, Italy
[b] State Key Laboratory of Fire Science, University of Science and Technology of China, Hefei, Anhui 230026, PR China
[c] National Synchrotron Radiation Laboratory, University of Science and Technology of China, Hefei, Anhui 230029, PR China

Article history:
Received 13 July 2013
Received in revised form 8 October 2013
Accepted 18 October 2013
Available online 12 November 2013

1. Introduction

Concerning the climate change, air pollution, and the shortage of transportation energy in the near future, biofuels, such as bio-ethanol and biodiesel, have been widely used as surrogates for traditional transportation fuels, because they are renewable and environmentally friendly. With the recent development of biological techniques, *n*-butanol, as a typical bio-alcohol, is considered as a potential fuel because of its advantages over smaller alcohols: higher energy density, higher mixing stability with fossil fuels, and higher suitability for conventional engines. Several experimental studies have been performed to investigate its combustion chemistry, including pyrolysis in flow reactors [1,2], oxidation in jet-stirred reactors [3–5], ignition delay time measurements in shock tubes [5–8], premixed [1,9–12] and non-premixed flames [13–15]. In the meantime, several kinetic models [1–3,5,6,9,10,13,16] have been developed to reproduce the combustion phenomenon of *n*-butanol and have been validated against experimental data, focusing on initial fuel decomposition and oxidation process. Oxygenated air pollutants, such as aldehydes, ketones, and ketene, as well as other major fuel decomposition intermediates, are usually reproduced satisfactorily by these models. However, the processes of benzene and PAH formation in the combustion of *n*-butanol and the interactions between *n*-butanol and hydrocarbons require further investigations.

Alcohols are considered environmentally friendly, because it is believed that they produce less PAHs in their combustion process than an equal amount of hydrocarbon with similar molecular structure does. Experiments carried out by Wu et al. [17] in premixed ethylene flames observed the reduction of aromatic species with the addition of ethanol. Similar tendencies were also found in the *n*-heptane premixed flames doped with methanol [18] and ethanol [19]. However, emission characteristics of higher alcohol/gasoline blends in engine achieved opposite conclusions. The net emissions of CO, CO_2 and organic matter hydrocarbon equivalent from the blends were very similar to those from neat gasoline [20]. In the premixed flames fueled with *n*-butanol ($\Phi = 1.70$)

* Corresponding authors. Address: Dipartimento di Chimica, Materiali e Ingegneria Chimica, Politecnico di Milano, Milano 20133, Italy. Fax: +39 027 0638173 (T. Faravelli), National Synchrotron Radiation Laboratory, University of Science and Technology of China, Hefei, Anhui 230029, PR China. Fax: +86 551 5141078 (F. Qi).
E-mail addresses: tiziano.faravelli@polimi.it (T. Faravelli), fqi@ustc.edu.cn (F. Qi).

and *n*-butane (Φ = 1.71) in similar flame conditions [11,21], similar mole fractions of cyclopentadiene and benzene were measured experimentally, which illustrated that the yields of PAHs may be equivalent in both flames. Meanwhile, a similar tendency of benzene concentration was observed in the comparison investigation of coflow methane flames doped with *n*-butanol and *n*-butane [15]. Therefore, it is important to better investigate the aromatic growth chemistry in the combustion of *n*-butanol, especially when it interacts with hydrocarbon fuels.

Coflow diffusion flames, which can produce large amount of PAHs, are suitable for the investigation of benzene formation and aromatic growth. The use of synchrotron VUV photoionization mass spectrometry (PIMS) has been proved to be very useful in the study of the detailed chemistry in these flames [14,22,23]. Combined with a powerful computational tool, laminarSMOKE [22,24], that is able to handle a detailed kinetic mechanism in multidimensional laminar flows, the aromatic growth chemistry can be studied quantitatively and accurately in coflow diffusion flames.

In this work, methane coflow diffusion flames doped with *n*-butanol were stabilized at atmospheric pressure. Methane is the simplest hydrocarbon. Its combustion kinetics has been investigated in many previous studies. Methane coflow diffusion flames without any doping fuels was studied experimentally with the same apparatus and simulated numerically with the same method before [22]. Therefore, methane is a suitable primary fuel to reduce the investigating complexity and focus on the *n*-butanol doping effect on PAH formation. Mole fractions of most stable flame species and some free radicals along the central axis of the flames were measured. Meanwhile, a kinetic mechanism, based on the previous alcohol mechanism [1] and aromatic mechanism of USTC [25], was developed to reproduce the experimental investigation, with the purpose to characterize the chemical interactions between butanol and methane. CFD calculations performed with laminarSMOKE code were able to provide not only the mole fractions of flame species over the whole flame field, but also the rate of production analysis along the central axis of the coflow flame. Key steps for the interaction between *n*-butanol and methane and the rate limiting steps in the formation of PAHs are identified.

2. Experimental methods

The experiments were carried out at National Synchrotron Radiation Laboratory in Hefei, China. The platform for the investigation of coflow diffusion flame with the method of molecular beam mass spectrometry (MBMS) combined with synchrotron vacuum ultraviolate photoionization (SVUV-PI) was reported in detail in previous studies [14]. As shown in Fig. 1, atmospheric pressure coflow non-premixed flames are stabilized on a burner with a 10 mm inner-diameter steel fuel tube located in the center of a 102 mm inner-diameter air tube. The fuel (CH_4 and C_4H_9OH), diluted gas (N_2), calibration gas (Ar) and air flow rates are presented in Table 1 with their purities of 99.995% for CH_4, 99.999% for N_2, 99.999% for O_2, 99.99% for Ar, and 99% for *n*-C_4H_9OH. Two different coflow flames were investigated in this experiment varied by different doping ratios of *n*-butanol in the fuel mixture (*Flame* 1: 3.90% C_4H_9OH and 25.46% CH_4; *Flame* 2: 1.95% C_4H_9OH and 33.27% CH_4), while the carbon flux was kept constant. The velocities of fuel mixture and air were 13.34 and 16.55 cm/s in both flames. The gas flow rates were regulated with mass flow controllers, except for *n*-butanol. *n*-Butanol was injected into a vaporizer with a chromatography pump, since it is liquid in room temperature. In order to avoid the liquefaction of *n*-butanol, the temperature of the vaporizer was kept at 30 K higher than its boiling point, and the temperature of the fuel mixture was also kept at 493 K during the experiment.

Flame species along the central axis of the flames were sampled, except in the region at the bottom of the flame, due to the shape limit of the sampling probe. In order to perform near threshold photoionization measurements and calculate the mole fractions of isomers, mass spectra were taken at the photon energies of 16.64, 15.20, 14.50, 12.00, 11.00, 10.00, and 9.50 eV. The detailed flame sampling and data reduction procedure were introduced in previous work [14]. The uncertainty of the experimental measurements with synchrotron vacuum ultraviolet photoionization mass spectrometry (SVUV-PIMS) is related to the probe sampling process and the photoionization cross sections adopted in the data reduction process. According to previous experimental investigations [14,22], the uncertainty of the mole fractions is within 20% for the flame species calculated with cold gas calibration, within 50% for the stable flame species with measured photoionization cross sections, and about a factor of 2 for the free radicals and the flame species with estimated photoionization cross sections.

3. Numerical methods and kinetic models

3.1. Numerical simulation methods

The laminar coflow flames were numerically simulated with the laminarSMOKE code [22,24]. It is a framework for the numerical simulation of multicomponent, compressible, thermally-perfect mixtures of gases with chemical reactions. It is based on the operator-splitting technique to deal with detailed kinetic schemes, and solves the conservation equations of total mass, momentum, individual species mass fractions and mixture energy. Both Fickian and thermal diffusion are taken into account [26]. An optically thin radiation model is included in the simulation and the Planck mean absorption coefficient is evaluated assuming that the only significant radiating species are H_2O, CO, CO_2 and CH_4 [27]. The transport properties of the species are taken from the Chemkin transport database [28] or estimated following the procedure described in [29].

Because of the axial symmetry of the system, the numerical calculations were performed on a stretched, two-dimensional,

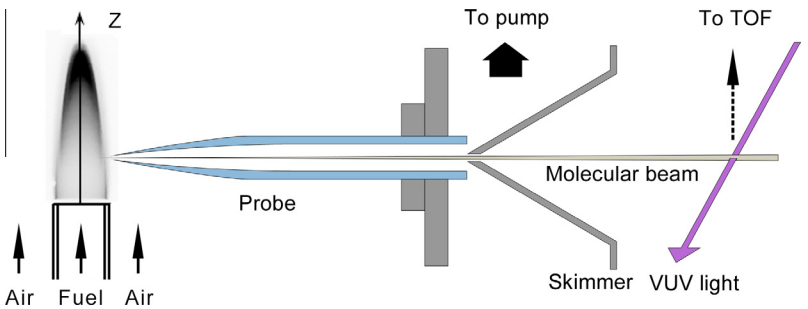

Fig. 1. A schematic sketch of the burner and the diagram of coflow flame analysis apparatus [14,22].

Table 1
Experimental conditions of coflow diffusion *n*-butanol doped methane flames (Unit: SCCM).

Name	Q_{air}	Q_{Ar}	Q_{N2}	Q_{CH4}	Q_{C4H9OH}
Flame 1	80,000	5.87	438	160	24.50
Flame 2	80,000	5.87	401	209	12.25

Note: Q_i is the flow rate of species i.

rectangular domain, with length of 250 mm and width of 53 mm. Considering the balance between the accuracy of numerical calculation and the cost of computational time, a mesh with 5604 cells was found fine enough for the purpose of the present work, also on the basis of previous studies [22]. The fuel stream was assumed at 493 K with a parabolic velocity profile, while the coflow air was imposed at ambient temperature with a flat velocity profile. The composition at the inlet boundary was fixed according to the data in Table 1.

3.2. Kinetic model construction

A kinetic scheme was developed in this work based on the former USTC alcohol mechanism, which was described in detail in the work of Cai et al. [1]. Comprehensive experimental data, including pyrolysis in flow reactors, oxidation in jet-stirred reactors, premixed flames, and ignition delay measurements in shock tubes in a wide temperature and pressure range, were used to validate the proposed mechanism. The purpose of the extension on the USTC alcohol mechanism in this work is to better characterize the benzene and PAH formation in the combustion of alcohols. Therefore, important aromatic growth pathways were included in this mechanism mainly according to the USTC aromatic mechanism (presented by Li et al. [25] in their work on the combustion of toluene). The thermodynamic properties of present model are taken from different thermodynamic databases [30] or previous models [6,10,16,31,32]. The present model consists of 216 species and 1235 reactions. Important modifications of the model (See Table 2) are presented in Section 3.3 and 3.4.

3.3. Decomposition mechanism of n-butanol

Unimolecular decomposition reactions of n-butanol are rather sensitive to the formation of important flame intermediates in diffusion flames. The rate constants of unimolecular decomposition reactions of n-butanol (R1–R4) adopted in the present model were checked with the recent reported experimental data [33] and theoretical calculations [1], as shown in Fig 2. The calculation carried out by Cai et al. [1] agrees very well with the values obtained in the shock tube study in the temperature and pressure range of 1126–1231 K and 1.3–6.5 bar by Rosado-Rayes et al. [33]. It confirms that

Table 2
Selected reactions in the present kinetic mechanism.[a]

	Selected reactions	*A*	*n*	*E*	Pressure (Torr)	Reference
1	$nC_4H_9OH = C_4H_8 + H_2O$	4.11×10^{83}	−20.67	102698	5	[1]
		3.25×10^{77}	−18.76	100769	30	[1]
		1.39×10^{73}	−17.43	98970	70	[1]
		2.215×10^{68}	−15.98	96774	200	[1]
		2.142×10^{60}	−13.60	92789	760	[1]
		4.829×10^{44}	−9.00	84357	7600	[1]
		1.24×10^{29}	−4.465	75432	76000	[1]
2	$nC_4H_9OH = nC_3H_7 + CH_2OH$	8.43×10^{101}	−25.53	122927	5	[1]
		1.19×10^{100}	−24.71	124635	30	[1]
		3.91×10^{97}	−23.86	124610	70	[1]
		2.11×10^{94}	−22.79	123938	200	[1]
		4.26×10^{87}	−20.71	121583	760	[1]
		4.45×10^{71}	−15.91	114141	7600	[1]
		4.28×10^{52}	−10.32	103881	76000	[1]
3	$nC_4H_9OH = C_2H_5 + CH_2CH_2OH$	2.44×10^{103}	−26.02	125685	5	[1]
		2.61×10^{102}	−25.42	128121	30	[1]
		2.84×10^{100}	−24.69	128556	70	[1]
		5.22×10^{97}	−23.76	128368	200	[1]
		4.61×10^{91}	−21.84	126653	760	[1]
		1.32×10^{76}	−17.12	119918	7600	[1]
		2.10×10^{56}	−11.28	109480	76000	[1]
4	$nC_4H_9OH = CH_3 + CH_2CH_2CH_2OH$	1.00×10^{103}	−26.05	125924	5	[1]
		1.46×10^{102}	−25.48	128466	30	[1]
		2.30×10^{100}	−24.80	129028	70	[1]
		4.48×10^{97}	−23.87	128871	200	[1]
		4.54×10^{91}	−21.96	127237	760	[1]
		1.19×10^{76}	−17.23	120522	7600	[1]
		1.67×10^{56}	−11.36	110115	76000	[1]
5	$C_3H_3 + C_3H_3 = C_6H_6$ (duplicate)	3.50×10^{65}	−15.90	27529		[45]
		2.40×10^{34}	−7.40	5058		[45]
6	$C_3H_3 + aC_3H_4 = C_6H_6 + H$	2.00×10^{13}	0.00	18000		[62–65]
7	$C_3H_3 + pC_3H_4 = C_6H_6 + H$	5.00×10^{11}	0.00	12000		[62]
8	$C_3H_3 + C_3H_3 = C_6H_5 + H$	2.02×10^{33}	−6.00	15940	30	[45]
		1.70×10^{48}	−9.97	36755	760	[39]
9	$C_6H_5CH_2 + C_2H_2 = C_9H_8 + H$	3.16×10^{4}	2.48	11061		[32]
10	$C_6H_5CH_2 + C_3H_3 = C_{10}H_8 + H + H$	3.00×10^{11}	0.00	0		[54]
11	$CH_3 + CH_3 = C_2H_5 + H$	4.99×10^{12}	0.10	10600		GRI
12	$H + pC_3H_4 = C_2H_2 + CH_3$	3.89×10^{10}	0.99	4114		[59]

[a] Units are s^{-1}, cm^3, and cal/mol.

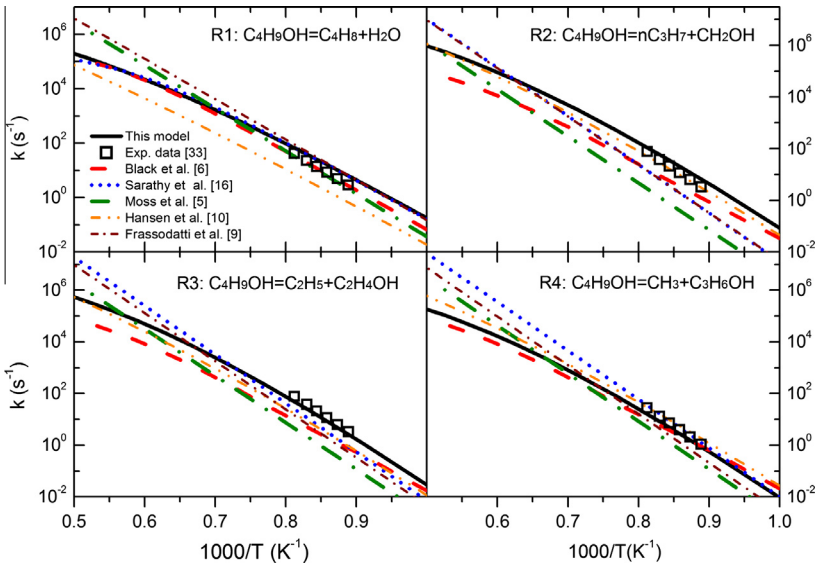

Fig. 2. Reaction rate constants of R1–R4 at 1 atm in this model, referred to Fig. 3 in [1], (models of Black et al. [6], Sarathy et al. [16], Moss et al. [5], Hansen et al. [10], Frassoldati et al. [9] and the experimental measurements by Rosado-Rayes et al. [33]).

the theoretical calculation by Cai et al. [1] is reasonable and accurate in certain extension into the typical reaction temperature range of the coflow flames. Therefore, their values are adopted in this study.

$$nC_4H_9OH = C_4H_8 + H_2O \quad (R1)$$

$$nC_4H_9OH = nC_3H_7 + CH_2OH \quad (R2)$$

$$nC_4H_9OH = C_2H_5 + CH_2CH_2OH \quad (R3)$$

$$nC_4H_9OH = C_3 + CH_2CH_2CH_2OH \quad (R4)$$

Another uncertainty in the n-butanol sub-mechanism is the H abstraction reactions of n-butanol by H-atoms. Figure 3 presents the selectivity of different H positions in the temperature range of 800–1500 K in the present model and the models established in the previous studies, including that of Black et al. [6], Moss et al. [5], Veloo et al. [31], Sarathy et al. [16], Harper et al. [2], Frassoldati et al. [9]. The diversity of the H abstraction selectivity in different models shows the entirely different understandings of the n-butanol decomposition mechanism. In general, the values in these models are close to each other, except those in the model of Moss et al. [5]. However, since there is lack of experimental and theoretical studies on the H abstraction reactions of n-butanol by H-atoms and the isomerization reactions among different C_4H_9O radicals, the rates of these reactions were modified in order to improve the accuracy of the modeling predictions, focusing on the importance of the different H positions (α, β, γ, δ, O). Experimental data of the n-butanol pyrolysis experiments at atmospheric pressure carried out by Harper et al. [2] and Cai et al. [1] were used to validate the modifications (see Section 4.1), respectively.

New experimental and theoretical studies on the H-atom abstraction of *n*-butanol by OH radical were recently reported by Pang et al. [34]. Their data showed good agreement with the experimental values reported by Vasu et al. [35] and the calculation results performed by Zhou et al. [36] in G3 potential energy surface. Detailed uncertainty analysis yielded an overall uncertainty in the measured rate constant of 20–23% in their

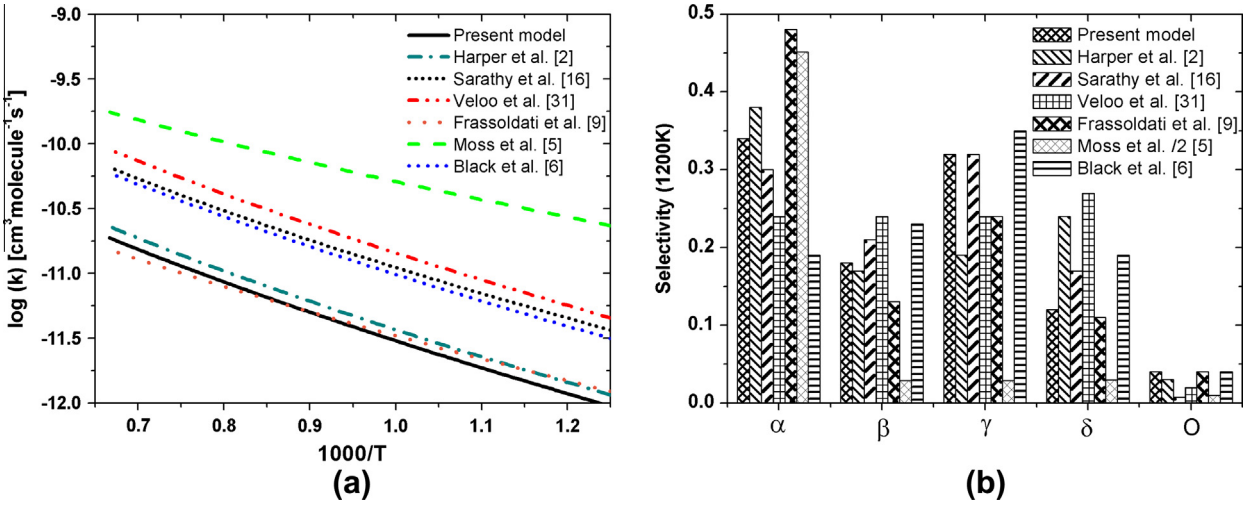

Fig. 3. (a) Total rate of reaction H + C_4H_9OH → Products in different mechanisms [2,5,6,9,16,31]. (b) Positions of the abstracted H-atom and selectivity of primary C_4H_9O radicals from H-abstraction reactions on *n*-butanol.

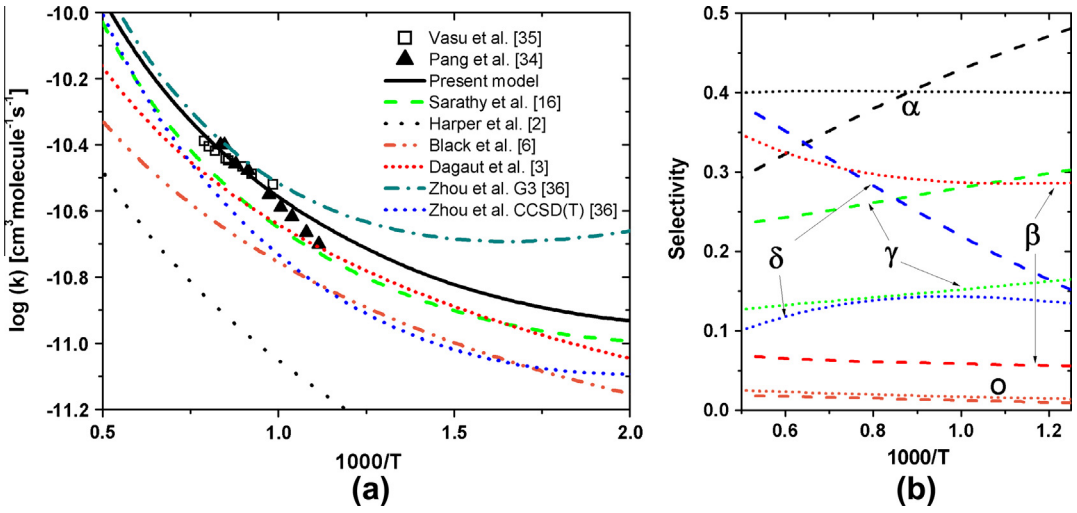

Fig. 4. (a) The comparison of the total reaction rate constants of OH radial H abstraction of *n*-butanol in the present model, (models of Sarathy et al. [16], Harper et al. [2], Black et al. [6], Dagaut et al. [3] and the experimental and theoretical of Vasu et al. [35], Pang et al. [34] and Zhou et al. [36]). (b) The H abstraction selectivity at different positions in the present model (dot lines) is compared to the theoretical investigation of Zhou et al. [36] (dash lines).

experimental temperature range (900–1200 K). The values adopted in the former USTC alcohol mechanism, which refer to the estimations of Sarathy et al. [16], agree well with the calculation of Zhou et al. in CCSD(T) level [36], but they are 2 times slower than the experimental data, as shown in Fig. 4. Therefore, a modification on the total reaction rate of OH-radical abstraction reactions has been performed in this work. Meanwhile, the selectivity in different H-atom positions of *n*-butanol by OH radical was also modified, in order to improve the predictions in the oxidation of *n*-butanol in JSR reactor (see Section 4.2) and premixed flames. The present study does not employ the rate constants calculated by Zhou et al. [36], but increases the selectivity of *β*-channel based on the evaluation of Sarathy et al. [16], because both the calculations of Zádor et al. [37] and Zhou et al. [36] were unable to accurately predict ignition delay times, as pointed out by Sarathy et al. [16] in their comprehensive study on the combustion of butanol isomers, and there was large discrepancy in the selectivity of different channels between these two theoretical studies.

3.4. Reactions for benzene and PAHs formation

The primary concern of the present study is better understand the formation progress of benzene, as well as PAH species especially indene and naphthalene. Important reaction pathways of the aromatic formation in the flame condition of the present study are discussed in the following paragraphs.

The most responsible source of benzene in *n*-butanol doped methane coflow flame was the recombination of propargyl radical with itself or other C3 species, including allene and propyne (R5–R8). The mechanism of this reaction system was investigated computationally by Miller et al. [38,39] on the potential energy surface of C_6H_6. Pressure dependent effect of these reactions was accounted in their calculation. Therefore, their calculated rate constant values were adopted in the present model. As a result, the recombination of propaygyl radicals yielding phenyl radical is the bottle-neck reaction of phenyl and benzene formation in this flame condition. The value of $1.7 \times 10^{48}[cm^3/mol/s]T^{-9.97}e^{-154.4[kJ/mol]/RT}$ at atmosphere pressure evaluated form the calculation of Miller et al. [39] was used. Figure 5 compares the rate constants obtained from the experimental measurements [40–43], the theoretical calculation [39] and the estimated values in previous models [44,45]. By fitting to a complex mechanism in different pressure range, Burcat et al. [46] gave the best estimation of $2 \times 10^{12}[cm^3/mol/s]$ $e^{-12.55[kJ/mol]/RT}$ in the condition of 1080–1550 K and 2–10 atm, while Rasmussen et al. [47] reported another value as $1.3 \times 10^{12}[cm^2/mol\ s]$ at 1400 K and 20 Torr. The values calculated by Miller et al. [39] at 30 Torr agreed well with the estimation of Rasmussen, which confirmed the accuracy of their calculation.

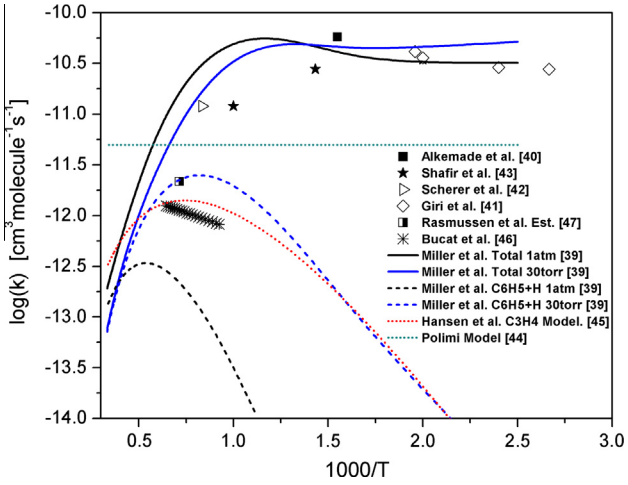

Fig. 5. Plot for the rate of C_3H_3 recombination reaction. Solid and open symbols denote low and atmosphere pressure experimental data for the total rate of all the channels [40–43]. The solid and dash lines denote the theoretical results for the total reaction and the phenyl + H channel, respectively, at 30 and 760 Torr [39]. The dot lines denote the typical evaluations in some models [44,45].

$$C_3H_3 + C_3H_3 = C_6H_6 \quad (R5)$$

$$C_3H_3 + aC_3H_4 = C_6H_6 + H \quad (R6)$$

$$C_3H_3 + pC_3H_4 = C_6H_6 + H \quad (R7)$$

$$C_3H_3 + C_3H_3 = C_6H_6 + H \quad (R8)$$

The rate constant of reaction R9 adopted in the present model was evaluated by Blanquart et al. [32], which agrees with the calculation results recommended by Vereecken et al. [48,49] in the temperature range of 200–2000 K. Matsugi et al. [50] also

estimated the rate constants of this reaction in their study on the pyrolysis of toluene based on the calculation of Kislov et al. [51] and Vereecken et al. [48,49] in the temperature range of 1000–4000 K. However it is an order of magnitude slower than the value used in the present model, and cannot reproduce the indene formation in this flame condition.

$$C_6H_5CH_2 + C_2H_2 = C_9H_8 + H \quad (R9)$$

$$C_6H_5CH_2 + C_3H_3 = C_{10}H_8 + 2H \quad (R10)$$

As suggested by McEnally et al. [52], benzyl radical can react with propargyl to form naphthalene. Blanquart et al. [32] estimated the rate constant of this reaction according to the reaction of ally radical with propargyl radical in their work. However, it seems the reaction is too active at low temperatures. Matsugi et al. [53] investigated the recombination of benzyl and propargyl radicals computationally, considering the pressure effect in the calculation. The pressure dependent rate constant value was presented in Chebyshev polynomial form, which was fitted by the authors at 10 Torr and 760 Torr for comparison. As shown in Fig. 6, the rate constants of the ring formation step are compared with the evaluation of Blanquart et al. [32]. A good agreement was found in shape between the estimation of Blanquart et al. [32] and the calculations of Matsugi et al. [53], but the estimated rates are faster in magnitudes. The rate constant of R10 was modified based on the estimation of D'Anna and Kent et al. [54]. Their estimation was well validated in their modeling investigation of aromatic formation in non-premixed methane flames. Therefore, it was adopted in the present model.

The mechanism for larger PAHs in the present model mainly refers to the recent model of Matsugi et al. [50] and Slavinskaya et al. [55,56], in which PAHs grow mainly based on HACA reactions [57] and the additional reaction of propargyl and allyl radicals [52,54]. The recombination reactions among large radicals, such as cyclopentadienyl, indenyl, naphthyl, etc., are also included in present model, which were proposed important pathways in the formation of large PAH in the work of Slavinskaya et al. [55,56]. The oxidation reactions of large PAH species mainly refer to the previous works of Blanquart et al. [32] and Slavinskaya et al. [55]. The thermodynamic properties for the different PAH molecules were taken from the compilation of Blanquart et al. [32].

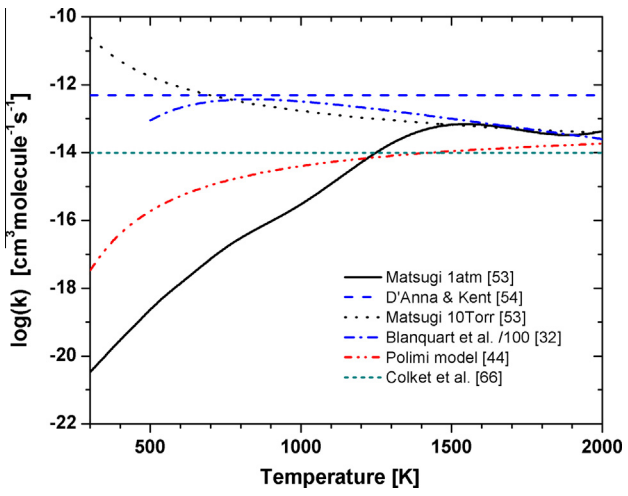

Fig. 6. Plot for the rate constants of $C_3H_3 + C_6H_5CH_2 = C_{10}H_8 + 2H$ (R10) reaction [32,44,53,54,66]. The solid and dash lines denote the values at atmosphere and low pressure.

4. Model validation through ideal reactor experiments

Coflow flame is a very complex combustion system, which is controlled by hydrodynamic, thermodynamic and chemical kinetics. It does not appear a proper way to validate a detailed kinetic mechanism directly with the coflow flame data and find out the chemical interaction on the formation of PAHs. Therefore, the proposed kinetic mechanism was validated first in ideal reactors in order to make sure that the fuel consumption process can be reproduced accurately. Only based on that, the chemical kinetics of PAH growth in the coflow flames could be discussed reasonably.

4.1. Butanol pyrolysis in flow reactors

The flow reactor is an important tool for studying the primary steps of the fuel decomposition reactions. Experimental data of the *n*-butanol pyrolysis experiments in flow reactor were reported by Harper et al. [2] (in the condition of 100% *n*-butanol) and Cai et al. [1] (in the condition of 3% *n*-butanol and 97% argon), respectively, measured with very different equipments. Their data were tested against many previous *n*-butanol models [2,9,13]. The present model was also validated against the *n*-butanol pyrolysis mechanism at 1 atm. The simulation was performed using the plug flow reactor code in the OpenSMOKE framework [58].

As shown in Fig. 7, the experimental data was measured by gas chromatography (GC) obtained from the work of Harper et al. [2]. The model in this study captures satisfactorily not only the fuel conversion but also the residence time, which reveals that the total *n*-butanol decomposition rate is well defined, including the unimolecular reactions and the H abstraction reactions by H-atom. Mass concentrations of the major decomposition species are plotted in the function of fuel conversion, mainly focusing on the selectivity of the fuel consumption channels. Primary intermediates yielded from the first-step decomposition of *n*-butanol are well reproduced in quantity and trend, including butene, propene, ethylene, acetaldehyde, water and methane.

The pyrolysis experiments of *n*-butanol performed from 5 Torr to atmospheric pressure were investigated in the work of Cai et al. [1], with the help of SVUV-PIMS technique. The data obtained at atmospheric pressure and 30 Torr was also reproduced by the present model. Figure 8 presents the comparison of the fuel conversion and intermediates productions at 1 atm, while the 30 Torr modeling data is provided in the Supplemental Material. As well as the prediction of the data of Harper et al., the fuel conversion and the mole fractions of main products are also in good agreement with the experimental measurements. Two isomers for C_2H_4O were distinguished as acetaldehyde and ethanol in Cai et al.'s work, and they were predicted very well by the present model. 1,3-Butadiene is perfectly predicted in this condition, comparing to the over prediction of 3 times in the experimental condition of Harper et al. (Fig. 7). In conclusion, the rates of the unimolecular decomposition reactions of *n*-butanol and H abstraction reactions by H-atom are well validated by the good agreement between the computational and experimental results in both the pyrolysis experiments.

4.2. Butanol oxidation in jet-stirred reactors

Dagaut and coworkers [3] presented experimental results for the oxidation of *n*-butanol in a jet-stirred reactor and a complete modeling analysis of the chemical mechanism. The experiments were conducted at atmosphere pressure in the temperature range of 800–1200 K and the residence time of approximately 0.07 s, in the condition from fuel lean to fuel rich (Φ = 0.5, 1.0, 2.0) conditions and high nitrogen dilution. These experimental data is very

useful in the validation of the detailed oxidation kinetics of the present model. The simulations were performed using the perfectly stirred reactor code in the OpenSMOKE framework [58] in steady-state conditions.

Detailed comparison on the profiles of several intermediates together with H_2, H_2O, CO, and CO_2 are presented in Figs. 9–11. The present model successfully reproduced the experimental data, especially the maximum mole fractions of most species and their trends with the fuel conversion in all the experimental conditions. However, the modeling prediction of the fuel consumption is always slower than the experimental measurement by about 15%. The Rate of Production (ROP) analysis shows that *n*-butanol is mainly consumed by the H abstraction of OH radical and some of the unimolecular reactions. According to Figs. 2 and 4, the total rate constant of the OH radical and *n*-butanol recombination reactions adopted in the present model fits very well the experimental measurements of Vasu et al. [35] and Pang et al. [34], while the rate constants of unimolecular reactions agree well with the recent experimental data reported by Rosado-Reyes et al. [33]. Therefore, the model predictions are considered in a good accuracy, since the reported uncertainty of the measurement in the jet-stirred reactor oxidation experiments is a factor of 2. The ignition delay time validation was also performed in this work (See Supplemental Material Fig. S2), which is important for the application of the kinetic scheme in IC engines.

5. Results and discussion

Two coflow diffusion flames (*Flame* 1 and *Flame* 2) were characterized both experimentally and numerically in this study. While the total gas flow rate and carbon flux were kept constant, the doping ratio of *n*-butanol was mainly varied to observe the impact on

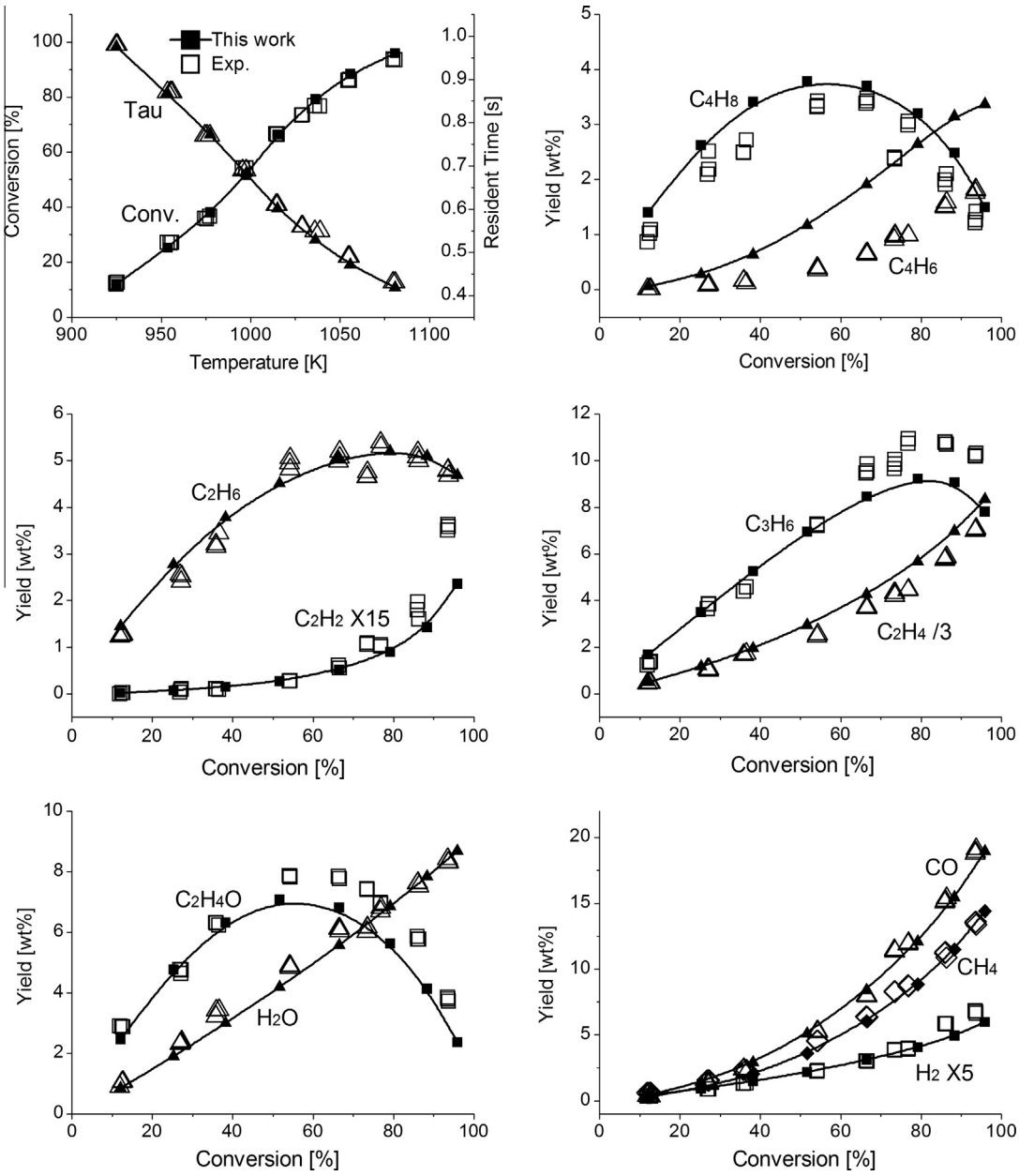

Fig. 7. Pyrolysis of *n*-butanol in the Ghent flow reactor [2]. Open symbols denote the experimental data [2]; solid symbols plus lines denote the predictions of the present model.

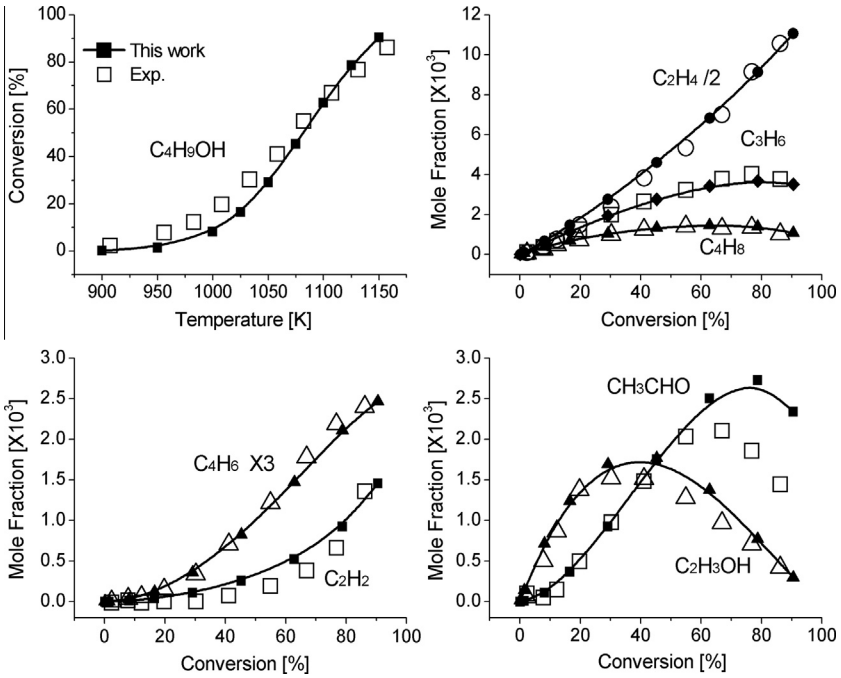

Fig. 8. Pyrolysis of *n*-butanol in the flow reactor at 1 atm [1]. Open symbols denote the experimental data from [1]; Solid symbols plus lines denote the predictions of the present model.

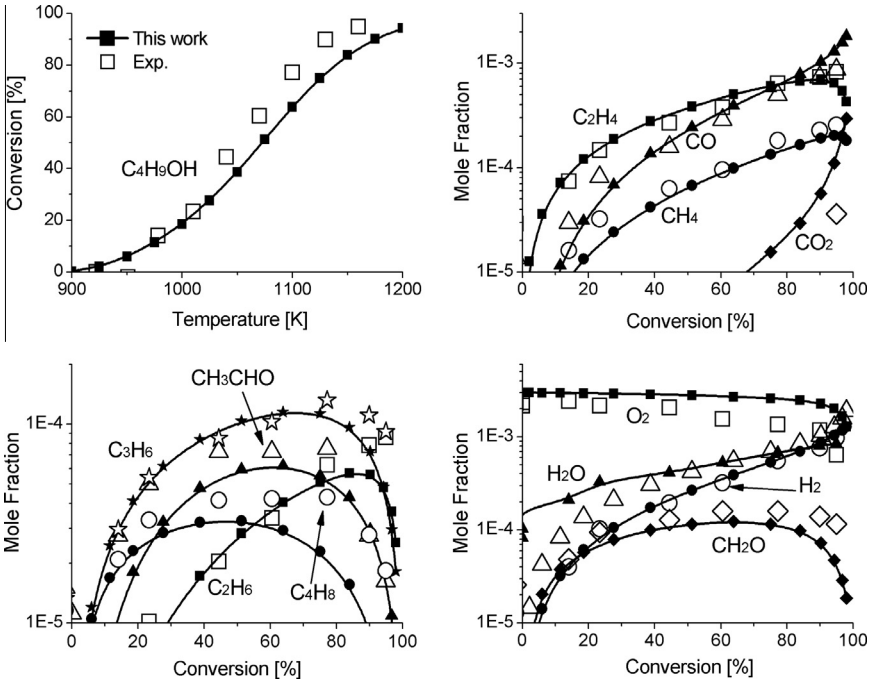

Fig. 9. Oxidation of *n*-butanol in the jet-stirred reactor [3] at atmosphere pressure and equivalent ratio $\Phi = 2.0$. Open symbols denote the experimental data [3]; solid symbols plus lines denote the predictions of the present model.

the flame structures, the flame conditions are presented in Table 1. Figure 12 shows the measurements and the predictions of the major combustion species (C_4H_9OH, CH_4, H_2, H_2O, CO, CO_2), dilution gas (N_2), and calibration gas (Ar) in the flames by the present model. The simulation results show good agreement with the experimental measurements for most species except CO, because of the limit of MS method. As known, the N_2 and CO peaks appear in very close positions in the mass spectrometry. In this experiment, the N_2 signal is so strong that it broadens to the peak position of CO, and consequently, impacts strongly on the evaluation of the CO mole fraction.

With an equivalent carbon flux in the inlet fuel gas, the mole fractions of the major combustion products in both flames seem consistent. A deviation of 1.9% in *n*-butanol doping ratio has no significant effect on the production of major products, but sufficiently large to influence the production of flame intermediates, especially

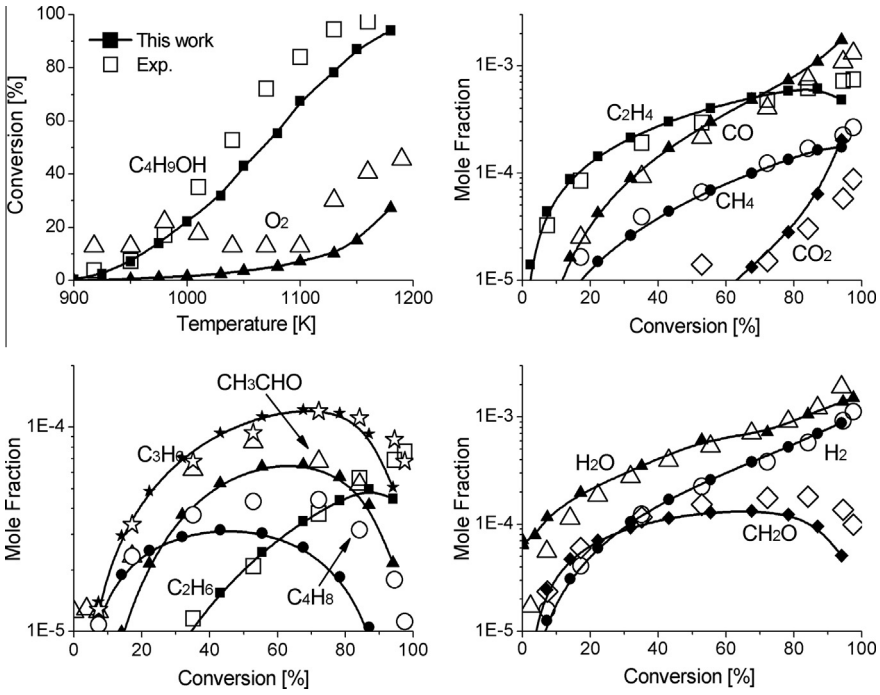

Fig. 10. Oxidation of *n*-butanol in the jet-stirred reactor [3] at atmosphere pressure and equivalent ratio $\Phi = 1.0$. Open symbols denote the experimental data [3]; solid symbols plus lines denote the predictions of the present model.

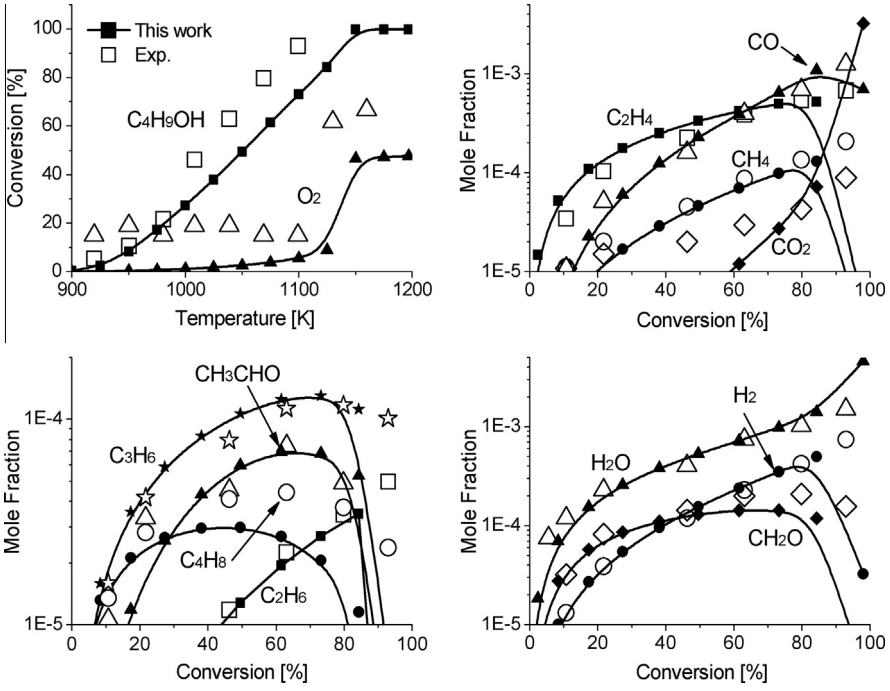

Fig. 11. Oxidation of *n*-butanol in the jet-stirred reactor [3] at atmosphere pressure and equivalent ratio $\Phi = 0.5$. Open symbols denote the experimental data [3]; solid symbols plus lines denote the predictions of the present model.

the benzene precursors and the aromatic species. As shown in Figs. 13 and 14, the mole fractions of the major benzene precursors, such as C3 and C4 hydrocarbons, increase significantly with the increasing doping ratio of *n*-butanol in the inlet fuel gas.

5.1. Fuel decomposition

Figure 13 compares the experimental and numerical mole fraction profiles of C4 hydrocarbons. The present model does an excellent job in the predictions. Butene isomers, including 1-butene and 2-butene, are over predicted by 20% in the maximum within the experimental measurement uncertainty. 1,3-Butadiene, that is one of the further decomposition products of butene, is well predicted too. It subsequently dehydrogenates to vinylacetylene, which is also well predicted with the change of butanol doping ratio.

Generally, the predictions of C4 species agree satisfactorily with the experimental measurements, while a slight over prediction can

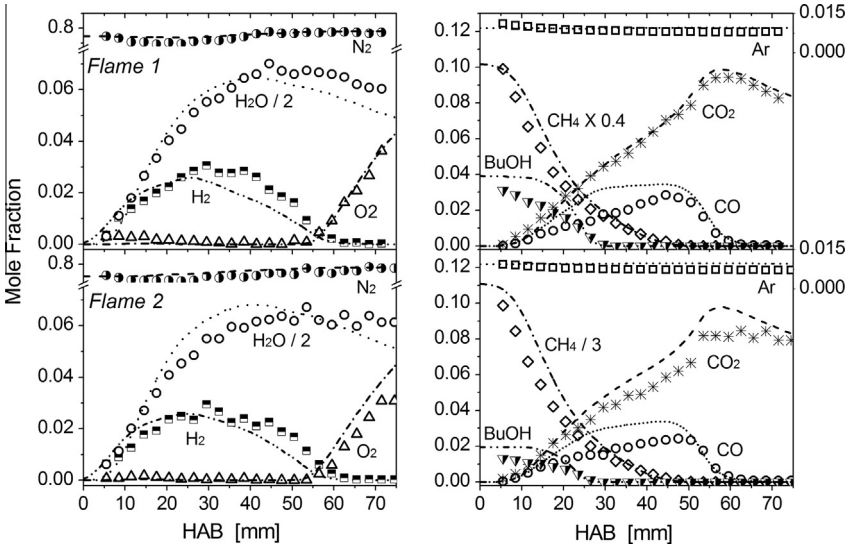

Fig. 12. Centerline mole fraction profile comparison between experimental measurements (symbols) and numerical simulations (lines) of major flame species in *Flame* 1 (upper) and *Flame* 2 (bottom). The mole fractions of argon are given on the right axis.

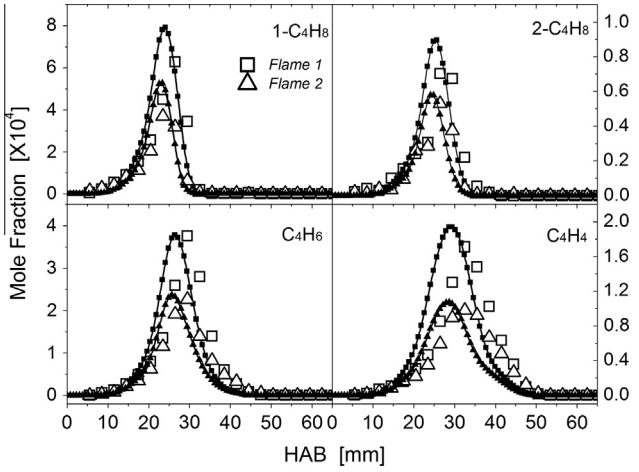

Fig. 13. Mole fraction comparison between experimental data (symbols) and numerical predictions (lines) of C4 hydrocarbon species, including 1-butene (1-C_4H_8), 2-butene (2-C_4H_8), isomers of C_4H_6 (C_4H_6), and vinylacetylene (C_4H_4).

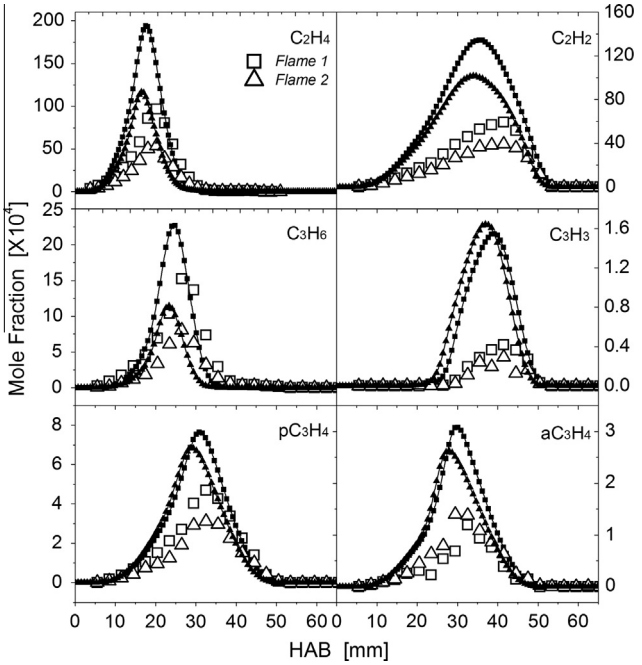

Fig. 14. Mole fraction comparison between experimental data (symbols) and numerical predictions (lines) of C2–C3 hydrocarbon species, including ethylene (C_2H_4), acetylene (C_2H_2), propene (C_3H_6), propargyl radical (C_3H_3), propyne (pC_3H_4), and allene (aC_3H_4).

be found in C2 and C3 hydrocarbons, especially ethylene and acetylene. The model tends to produce too much C2 and C3 species, except propene. The modeling results of propyne, allene, and ethylene are within 2 times of the experimental data. The predictions of propargyl radical are slightly worse, around 3.5 times, that maybe caused by radical annihilation in the sampling probe. C_3H_3 is mainly formed from propyne and allene, and is the main precursor of aromatic species. A deviation about 3 times in the mole fraction of acetylene can be also found between the measurement and the simulation, which in turn leads to the over prediction of propyne. Besides these, the impact of the *n*-butanol doping ratio on the quantities of intermediates is well captured by the model.

Figure 15 presents the detailed decomposition pathways of *n*-butanol in *Flame* 1. The ROP analysis of *Flame* 1 shows that unimolecular decomposition consumes 54.5% of *n*-butanol, comparing to 45.0% consumed by H-abstraction reactions. Cai et al. [1] pointed out the importance of unimolecular decomposition reactions in their study of *n*-butanol pyrolysis. These reactions also play a dominant role in the *n*-butanol consumption in the coflow flames, which is also summarized in McEnally et al.'s [15] pioneer experimental comparison research on the butanol isomers doped methane coflow flames. 1-Butene is a major stable intermediate product mainly formed directly through the reaction $C_4H_9OH = 1-C_4H_8 + H_2O$ (R1), which contributes 16.6% in fuel consumption. 2-Butene, 1,3-butadiene, and vinylacetylene are the isomerization or further decomposition products of 1-butene.

Beside 1-butene, the map of Fig. 15 also illustrates that propene and ethylene are important intermediates. The main precursors of ethylene are the C_2H_5, nC_3H_7, and C_2H_4OH radicals, which are dominantly yielded from the recombination of methyl radical ($CH_3 + CH_3 = C_2H_5 + H$ (R11)) and the unimolecular reactions of R2 and R3. αC_4H_9OH radical, formed from the H abstraction

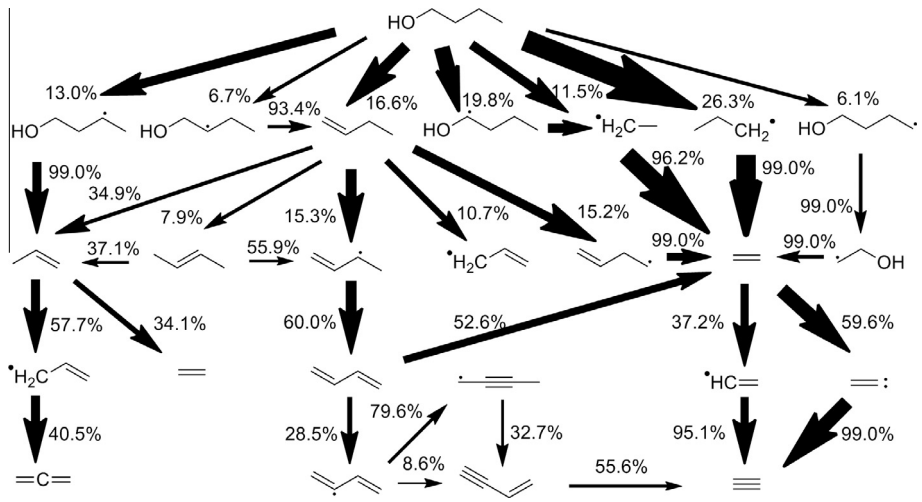

Fig. 15. Major reaction pathways in *Flame* 1. The thickness of the arrow is proportional to the carbon flux of the pathway, and the number beside denotes the conversion rate of each reaction.

reaction of *n*-butanol, decomposes to C_2H_5 radical in the following β-scission, which plays an additional role in the formation of ethylene. Ethylene mainly forms acetylene via vinyl and vinylidene radical channels. The pathway consumes about 90% of ethylene in *Flame* 1. Propene, which forms allyl radical and allene, is mainly formed via H-abstraction of *n*-butanol through the β-scission of γC_4H_8OH radical. Subsequently, allene and propyne can quickly isomerize to each other and produce propargyl radical, which significantly contributes to the benzene formation. However, it is a minor pathway in the formation of propyne. Because of the high mole fraction of methyl radical provided by methane, the dominant pathway in coflow methane flames is the reaction $pC_3H_4 + H = C_2H_2 + CH_3$ (R12). The importance of this reaction was concluded by Cuoci et al. in their study on CH_4/C_2H_4 coflow flames [24]. This reaction relates the combustion of methane and *n*-butanol in the cooperation of benzene formation, as shown in Fig. 16. Since propyne mainly forms propargyl radical in its further reactions in this flame condition, the doping of *n*-butanol increases the concentration of ethylene in the flames, and consequently enhances the benzene formation rate via the following reactions sequence: $C_2H_4 \rightarrow C_2H_3 \rightarrow C_2H_2 \rightarrow pC_3H_4 \rightarrow C_3H_3 \rightarrow C_6H_6$.

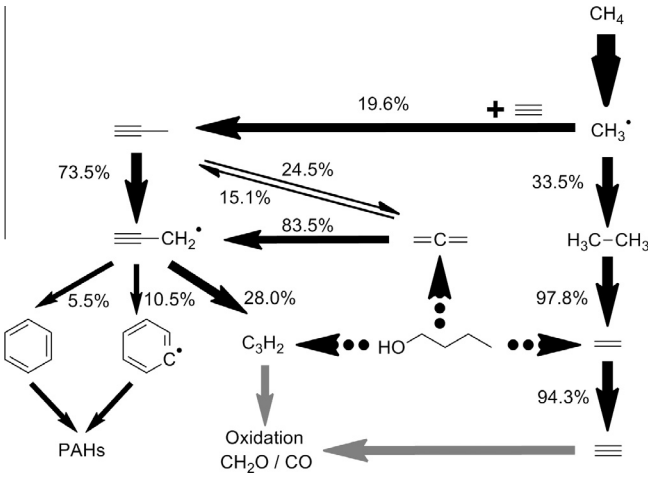

Fig. 16. Major reaction pathways of methane in *Flame* 1. The thickness of the arrow is proportional to the carbon flux of the pathway, and the number beside denotes the conversion rate of each reaction. Dot arrows highlight the interactions between n-butanol and methane in combustion; and gray arrows highlight the oxidation pathways.

5.2. Aromatic hydrocarbon formation

The variations of the aromatic formation in the flames with different *n*-butanol doping ratios were captured by the present model. As shown in Fig. 17, the mole fractions of aromatic species increase while the doping ratio increases. A slight over prediction of monocyclic aromatic hydrocarbons (MAHs) in the flames can be found in model predictions. Benzene is over predicted by a factor of 2, while for other species, including toluene, styrene, and phenylacetylene, the deviations between the experiments and simulations are within 50%. In general, the predictions obtained from the present model agree satisfactorily with the experimental measurements.

Indene and naphthalene are also well reproduced by the present model, as shown in Fig. 18. However, large deviations exist between the simulation results and the experimental data of larger aromatic species. $C_{12}H_8$ (acenaphthylene) and $C_{14}H_{10}$ (phenanthrene, anthracene and 1-ethenylacenaphthylene) were over predicted by around 3 times. A novel observation of $C_{10}H_6$ in this study (as shown in Fig. 18), which may be diethynylbenzene, makes the former pathway reasonable. Experimental data reveal the possible existence of the acetylenylphenyl radical, although

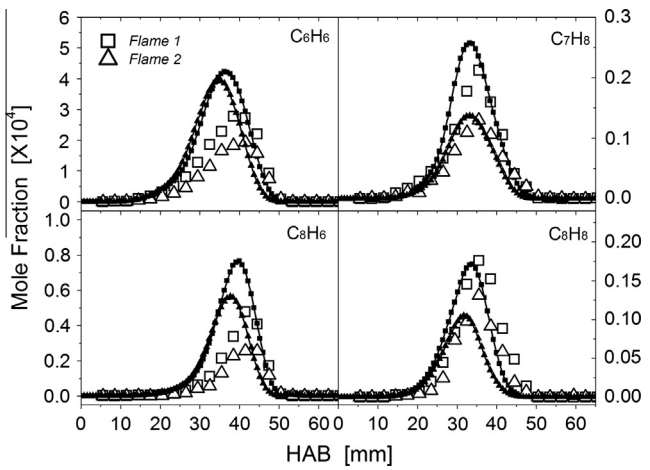

Fig. 17. Mole fraction comparison between experimental data (symbols) and numerical predictions (lines) of MAHs, including benzene (C_6H_6), toluene (C_7H_8), styrene (C_8H_8), and phenylacetylene (C_8H_6).

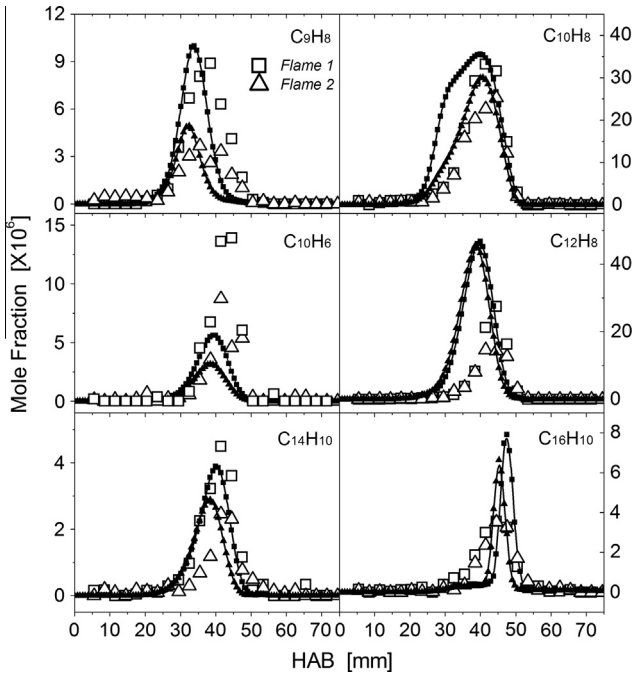

Fig. 18. Mole fractions comparison between experimental data (symbols) and numerical predictions (lines) of PAHs, including C_9H_8 (indene), $C_{10}H_8$ (naphthalene), $C_{10}H_6$ (diethynylbenzene), $C_{12}H_8$ (acenaphthylene), $C_{14}H_{10}$ (phenanthrene, Anthracene and 1-ethenylacenaphthylene), and $C_{16}H_{10}$ (pyrene and fluoranthene).

the low accuracy of the photoionization efficiency (PIE) measurement in these conditions makes this result unsure. The kinetic mechanism under predicts the mole fractions of $C_{16}H_{10}$ species (pyrene and fluoranthene) and does not capture their consumption correctly, which indicates that the model needs to be further developed in their formation and consumption routes toward heavier PAHs and soot. Generally, considering the complexity of the flame and the issue of the entrainment rate, the level of the agreement is satisfactory.

Figure 19 shows the major pathways of PAH formation in *Flame* 1. Benzene and phenyl radical are the key PAH growth points in the flame. Toluene, phenylacetylene and styrene are yielded from phenyl radical via the addition of methyl, acetylene and ethylene, while phenyl radical is mainly formed via the recombination reaction of propargyl radical (R9). Therefore, the over prediction of

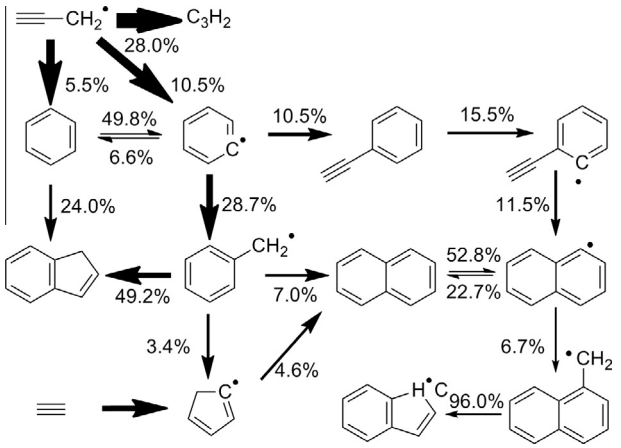

Fig. 19. Reaction pathways leading to the formation of PAHs in *Flame* 1. The thickness of the arrow is proportional to the carbon flux of the pathway, and the number beside denotes the conversion rate of each reaction.

propargyl radical and propyne leads to the over prediction of MAHs directly. A sensitivity analysis of the benzene formation was conducted in a counter flow diffusion flame [22] with the same flame condition of *Flame* 1. As shown in Fig. 20, R1, R2, R12, and R8 are the most sensitive reactions in the formation of benzene, while R12 and R8 are also the most sensitive ones for phenyl radical. Combining with the reaction pathway analysis in Figs. 15 and 19, it is evident that R12 and R8 are the rate-control reactions in the formation of MAH species. Other benzene formation pathways such as C4 + C2 reactions and $C_3H_3 + aC_3H_5$ reaction that also proposed in the present model provide minor contributions in this flame condition. R12 is the major propyne formation pathway in the flames, which produces the main benzene precursor, propargyl radical. The rate of R12 used in the present model is evaluated from the calculation of Miller et al. [59] on a aC_3H_5 potential energy surface in 2008. R8, the recombination of propargyl radical, is the dominant pathway in forming phenyl radical, subsequently controls the rate of benzene formation. The rate constants calculated by Miller et al. [38,39] are adopted in the present model accounting for the pressure dependence effect of R8. Therefore, in this flame condition, a satisfied agreement between the experimental measurements and the predictions can be observed in MAH intermediates.

Benzyl radical, which is formed via the recombination of phenyl and methyl radicals, plays an important role in the formation of naphthalene and indene, subsequently, leads the aromatics growing to larger PAHs and soot. The recombination reaction of benzyl and propargyl radical (R10) contributes for 31.2% to the naphthalene formation in *Flame* 1. Another efficient naphthalene formation channel is the recombination reaction of cyclopentadienyl radical, which yields a contribution of 30.1% as similar channel as R10. The recombination reactions among phenylacetylene, acetylenylphenyl radical, acetylene, and vinyl radical are minor naphthalene formation routes. The detailed information for the naphthalene formation from benzyl radical can be found in [25], in which the recombination reaction of benzyl and propargyl radical (R10) was found to be the key reaction. A sensitivity analysis from the counter-flow flame was also performed in conditions similar to *Flame* 1. Among the listed reactions in Fig. 21, the rate-controlling reaction is obviously R10, which is not only the dominant naphthalene formation channel, but also the most sensitive reaction in this process. Besides, the reaction that contributes to the formation of propargyl radical as well as of benzyl radical reveals a positive sensitivity in naphthalene formation ($pC_3H_4 + H = C_3H_3 + H_2$ and $C_6H_5CH_2 + H = C_6H_5 + CH_3$). The unimolecular decomposition reaction of *n*-butanol yielding 1-butnene (R1) has a positive sensitivity too, because most of 1-butene will decompose to propargyl radical in this sequence: $C_4H_8 \rightarrow aC_3H_5 \rightarrow aC_3H_4 \rightarrow C_3H_3$. The results of sensitivity analysis presented in Figs. 20 and 21 further support the conclusions from the aromatic formation path analysis.

Indene is mainly formed from two pathways in this condition: the recombination reaction of benzyl radical and acetylene contributes the major production, while the reaction of benzene and propargyl radical is an additional channel. Compared to the former pathways, radical recombination reaction between phenyl and propargyl radical provide a minor route in indene formation. Naphthalenyl radical combines with H atom to form naphthalene, competing with the pathway of methyl radical addition reaction to form naphthylmethyl radical. The ring shrinking reaction of the yielded naphthylmethyl radical, which forms indenyl radical, is an additional formation pathway for indene. The rate constant of reaction R9 adopted in the present model is evaluated by Blanquart et al. [32], giving a good agreement between modeling predictions and experimental measurements. The value proposed by Matsugi et al. [50] is much slower than the value used in the present model,

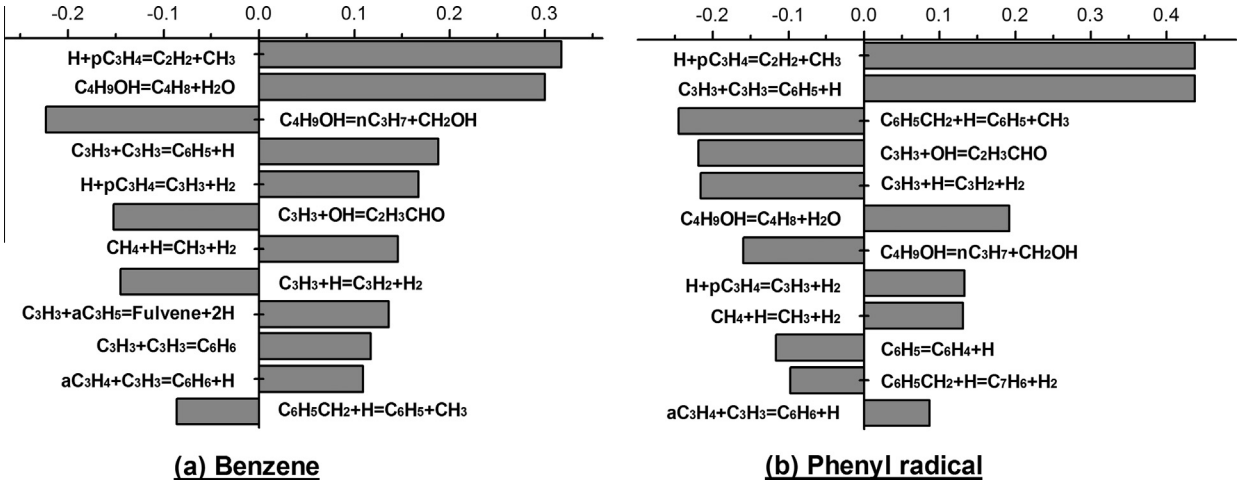

Fig. 20. Sensitivity analysis for benzene and phenyl radical formation in a counter flow diffusion flame (conditions of inlet reactant similar to those of *Flame* 1).

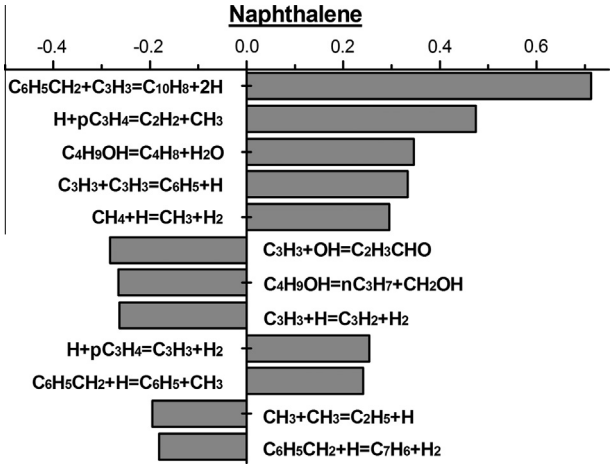

Fig. 21. Sensitivity analysis for naphthalene formation in a counter flow diffusion flame (conditions of inlet reactant similar to those of *Flame* 1).

which cannot reproduce the indene formation in this flame condition.

Novel PAH formation routes were added to the model, referred to the recent two- and three-ring aromatics formation mechanism developed in the pyrolysis study of toluene [50] and the pathways proposed by Shukla et al. [60,61] in the acetylene pyrolysis investigation. Large PAH species, including phenanthrene, anthracene, pyrene, and fluoranthene, were not well predicted by the present model. It may be caused both by the accuracy of the experimental measurement in low mole fraction and by the lack of the theoretical calculation information in PAH formation. ROP analysis based on the present model illustrates that large PAH species are mainly grown based on indenyl and naphthalenyl radicals. Further theoretical investigation on the growth of large PAH species is demanded to reproduce their formation accurately in wide range of combustion condition.

6. Conclusions

In this work, two coflow methane flames doped with *n*-butanol were studied both experimentally and numerically. Synchrotron VUV photoionization mass spectrometry technique was used to identify the flames species and measure them quantitatively. A novel *n*-butanol kinetic mechanism extended from the previous USTC alcohol mechanism was developed, giving a better characterize on the benzene and PAH formation in the combustion of alcohols. Numerical simulations with detailed kinetics and transfer properties were performed to better investigate and interpret the experimental measurements. With particular attention on the formation of benzene and PAHs, the interaction between *n*-butanol and methane in the fuel decomposition and aromatic formation process was analyzed in detail. The impact of the doping of *n*-butanol is found to be pronounced for benzene formation by increasing the mole fractions of C2 species, which subsequently lead to the increase of propyne and propargyl radical. Benzyl radical, formed from the recombination of phenyl and methyl radical, is the main precursor of naphthalene. Meanwhile, the pathway that forms naphthalene from phenylacetylene plays an additional role. Indene is formed in a limited amount, compared to that of naphthalene, mainly through the reaction between benzene and propargyl radical. Larger aromatics, such as $C_{12}H_8$, $C_{14}H_{10}$ and $C_{16}H_{10}$ isomers, were measured and modeled in this study, but the scheme needs to be further developed in the chemistry of large aromatics growth. More detailed PAH chemistry and the incorporation of additional pathways towards aromatic formations seem promising for improving model predictions.

Acknowledgments

Authors are grateful for funding supports from National Basic Research Program of China (973 Program) (2013CB834602), Natural Science Foundation of China (50925623 and 51127002), and Chinese Academy of Sciences. Hanfeng Jin is grateful for the joint PhD scholarship funded by China Scholarship Council.

Appendix A. Supplementary material

Supplementary data associated with this article can be found, in the online version.

References

[1] J. Cai, L. Zhang, F. Zhang, Z. Wang, Z. Cheng, W. Yuan, F. Qi, Energy Fuels 26 (2012) 5550–5568.
[2] M.R. Harper, K.M. Van Geem, S.P. Pyl, G.B. Marin, W.H. Green, Combust. Flame 158 (2011) 16–41.
[3] P. Dagaut, S.M. Sarathy, M.J. Thomson, Proc. Combust. Inst. 32 (2009) 229–237.
[4] P. Dagaut, C. Togbe, Fuel 87 (2008) 3313–3321.
[5] J.T. Moss, A.M. Berkowitz, M.A. Oehlschlaeger, J. Biet, V. Warth, P.A. Glaude, F. Battin-Leclerc, J. Phys. Chem. A 112 (2008) 10843–10855.

[6] G. Black, H.J. Curran, S. Pichon, J.M. Simmie, V. Zhukov, Combust. Flame 157 (2010) 363–373.
[7] K.A. Heufer, R.X. Fernandes, H. Olivier, J. Beeckmann, O. Röhl, N. Peters, Proc. Combust. Inst. 33 (2011) 359–366.
[8] I. Stranic, D.P. Chase, J.T. Harmon, S. Yang, D.F. Davidson, R.K. Hanson, Combust. Flame 159 (2012) 516–527.
[9] A. Frassoldati, R. Grana, T. Faravelli, E. Ranzi, P. Oßwald, K. Kohse-Höinghaus, Combust. Flame 159 (2012) 2295–2311.
[10] N. Hansen, M.R. Harper, W.H. Green, Phys. Chem. Chem. Phys. 13 (2011) 20262–20274.
[11] P. Oßwald, H. Güldenberg, K. Kohse-Höinghaus, B. Yang, T. Yuan, F. Qi, Combust. Flame 158 (2011) 2–15.
[12] B. Yang, P. Oßwald, Y. Li, J. Wang, L. Wei, Z. Tian, F. Qi, K. Kohse-Höinghaus, Combust. Flame 148 (2007) 198–209.
[13] R. Grana, A. Frassoldati, T. Faravelli, U. Niemann, E. Ranzi, R. Seiser, R. Cattolica, K. Seshadri, Combust. Flame 157 (2010) 2137–2154.
[14] H. Jin, Y. Wang, K. Zhang, H. Guo, F. Qi, Proc. Combust. Inst. 34 (2013) 779–786.
[15] C.S. McEnally, L.D. Pfefferle, Proc. Combust. Inst. 30 (2005) 1363–1370.
[16] S.M. Sarathy, S. Vranckx, K. Yasunaga, M. Mehl, P. Oßwald, W.K. Metcalfe, C.K. Westbrook, W.J. Pitz, K. Kohse-Höinghaus, R.X. Fernandes, H.J. Curran, Combust. Flame 159 (2012) 2028–2055.
[17] J. Wu, K.H. Song, T. Litzinger, S.-Y. Lee, R. Santoro, M. Linevsky, M. Colket, D. Liscinsky, Combust. Flame 144 (2006) 675–687.
[18] G. Chen, W. Yu, J. Fu, J. Mo, Z.H. Huang, J.Z. Yang, Z.D. Wang, H.F. Jin, F. Qi, Combust. Flame 159 (2012) 2324–2335.
[19] J. Song, C. Yao, S. Liu, H. Xu, Energy Fuels 22 (2008) 3806–3809.
[20] M. Gautam, D. Martin II, D. Carder, Proc. Inst. Mech. Eng. 214 (2000) 165–182.
[21] P. Oßwald, K. Kohse-Höinghaus, U. Struckmeier, T. Zeuch, L. Seidel, L. Leon, F. Mauss, Z. Physik, Chemie 225 (2011) 1029–1054.
[22] A. Cuoci, A. Frassoldati, T. Faravelli, H. Jin, Y. Wang, K. Zhang, P. Glarborg, F. Qi, Proc. Combust. Inst. 34 (2013) 1811–1818.
[23] F. Qi, Proc. Combust. Inst. 34 (2013) 33–63.
[24] A. Cuoci, A. Frassoldati, T. Faravelli, E. Ranzi, Combust. Flame 160 (2013) 870–886.
[25] Y. Li, J. Cai, L. Zhang, T. Yuan, K. Zhang, F. Qi, Proc. Combust. Inst. 33 (2011) 593–600.
[26] S. Chapman, T.G. Cowling, The Mathematical Theory of Non-Uniform Gases, Cambrige University Press, Cambrige, 1970.
[27] R.J. Hall, J. Quant. Spectrosc. Radiat. Transfer 49 (1993) 517–523.
[28] R.J. Kee, J. Warnatz, J.A. Miller, Chemkin II: A Fortran Chemcal Kinetics Package for the Evaluation of Gas-Phase Viscosities, Conductivities and diffusion Coefficient, Sandia National Laboratory, 1983.
[29] H. Wang, M. Frenklach, Combust. Flame 96 (1994) 163–170.
[30] E. Goos, A. Burcat, B. Ruscic, Ideal Gas Thermochemical Database with Updates from Active Thermochemical Table, 2005, ftp://ftp.technion.ac.il/pub/supported/aetdd/thermodunamics.
[31] P.S. Veloo, F.N. Egolfopoulos, Proc. Combust. Inst. 33 (2011) 987–993.
[32] G. Blanquart, P. Pepiot-Desjardins, H. Pitsch, Combust. Flame 156 (2009) 588–607.
[33] C.M. Rosado-Reyes, W. Tsang, J. Phys. Chem. A 116 (2012) 9825–9831.
[34] G.A. Pang, R.K. Hanson, D.M. Golden, C.T. Bowman, J. Phys. Chem. A 116 (2012) 2475–2483.
[35] S.S. Vasu, D.F. Davidson, R.K. Hanson, D.M. Golden, Chem. Phys. Lett. 497 (2010) 26–29.
[36] C.-W. Zhou, J.M. Simmie, H.J. Curran, Combust. Flame 158 (2011) 726–731.
[37] J. Zádor, J.A. Miller, 7th US Nat. Tech. Meet. Combust. Inst. (2011).
[38] J.A. Miller, S.J. Klippenstein, J. Phys. Chem. A 105 (2001) 7254–7266.
[39] J.A. Miller, S.J. Klippenstein, J. Phys. Chem. A 107 (2003) 7783–7799.
[40] U. Alkemade, K.H. Homann, Z. Physik, Chemie 161 (1989) 19–34.
[41] B.R. Giri, H. Hippler, M. Olzmann, A.N. Unterreiner, Phys. Chem. Chem. Phys. 5 (2003) 4641–4646.
[42] S. Scherer, T. Just, P. Frank, Proc. Combust. Inst. 28 (2000) 1511–1518.
[43] E.V. Shafir, I.R. Slagle, V.D. Knyazev, J. Phys. Chem. A 107 (2003) 8893–8903.
[44] http://creckmodeling.chem.polimi.it/index.php/kinetic-schemes.
[45] N. Hansen, J.A. Miller, P.R. Westmoreland, T. Kasper, K. Kohse-Hoinghaus, J. Wang, T.A. Cool, Combust. Flame 156 (2009) 2153–2164.
[46] A. Burcat, M. Dvinyaninov, Int. J. Chem. Kinet. 29 (1997) 505–514.
[47] C.L. Rasmussen, M.S. Skjøth-Rasmussen, A.D. Jensen, P. Glarborg, Proc. Combust. Inst. 30 (2005) 1023–1031.
[48] L. Vereecken, H.F. Bettinger, J. Peeters, Phys. Chem. Chem. Phys. 4 (2002) 2019–2027.
[49] L. Vereecken, J. Peeters, Phys. Chem. Chem. Phys. 5 (2003) 2807–2817.
[50] A. Matsugi, A. Miyoshi, Proc. Combust. Inst. 34 (2013) 269–277.
[51] V.V. Kislov, N.I. Islamova, A.M. Kolker, S.H. Lin, A.M. Mebel, J. Chem. Theor. Comput. 1 (2005) 908–924.
[52] C.S. McEnally, L.D. Pfefferle, B. Atakan, K. Kohse-Hoinghaus, Prog. Energy Combust. Sci. 32 (2006) 247–294.
[53] A. Matsugi, A. Miyoshi, Int. J. Chem. Kinet. 44 (2012) 206–218.
[54] A. D'Anna, J.H. Kent, Combust. Flame 132 (2003) 715–722.
[55] N.A. Slavinskaya, P. Frank, Combust. Flame 156 (2009) 1705–1722.
[56] N.A. Slavinskaya, U. Riedel, S.B. Dworkin, M.J. Thomson, Combust. Flame 159 (2012) 979–995.
[57] M. Frenklach, H. Wang, Proc. Combust. Inst. 23 (1991) 1559–1566.
[58] A. Cuoci, A. Frassoldati, T. Faravelli, E. Ranzi, Combust. Flame 156 (2009) 2010–2022.
[59] J.A. Miller, J.P. Senosiain, S.J. Klippenstein, Y. Georgievskii, J. Phys. Chem. A 112 (2008) 9429–9438.
[60] B. Shukla, M. Koshi, Combust. Flame 159 (2012) 3589–3596.
[61] B. Shukla, M. Koshi, Phys. Chem. Chem. Phys. 12 (2010) 2427–2437.
[62] T. Faravelli, A. Goldaniga, L. Zappella, E. Ranzi, P. Dagaut, M. Cathonnet, Proc. Combust. Inst. 28 (2000) 2601–2608.
[63] Y. Hidaka, T. Nakamura, A. Miyauchi, T. Shiraishi, H. Kawano, Int. J. Chem. Kinet. 21 (1989) 643–666.
[64] C.H. Wu, R.D. Kern, J. Phys. Chem. 91 (1987) 6291–6296.
[65] P. Dagaut, M. Cathonnet, Combust. Sci. Technol. 137 (1998) 237–275.
[66] M.B. Colket, D.J. Seery, Proc. Combust. Inst. 25 (1994) 883–892.